

MBG/ PGA-PCL composite scaffolds provide highly tunable degradation and osteogenic features

Jiangfeng Li^{a,1}, Chunyi Wang^{b,1}, Guoxing Gao^a, Xing Yin^c, Ximing Pu^a, Bing Shi^b, Yang Liu^d, Zhongbing Huang^a, Juan Wang^a, Jingtao Li^{b,**}, Guangfu Yin^{a,*}

^a College of Biomedical Engineering, Sichuan University, Chengdu, 610065, PR China

^b State Key Laboratory of Oral Diseases, National Clinical Research Center for Oral Diseases, Department of Oral and Maxillofacial Surgery, West China Hospital of Stomatology, Sichuan University, Chengdu, 610041, PR China

^c State Key Laboratory of Oral Diseases, National Clinical Research Center for Oral Diseases, Department of Orthodontics, West China Hospital of Stomatology, Sichuan University, Chengdu, 610041, PR China

^d Shandong Provincial Key Laboratory of Biomedical Polymers, Shandong Academy of Pharmaceutical Sciences, Jinan, 250101, PR China

ARTICLE INFO

Keywords:

Mesoporous bioactive glasses
Poly(caprolactone-co-glycolide)
Osteogenic differentiation
Bone repair

ABSTRACT

It remains a challenge to achieve satisfactory balance between biodegradability and osteogenic capacity in biosynthetic bone grafts. In this study, we aimed to address this challenge by incorporating mesoporous bioactive glass (MBG) into poly(caprolactone-co-glycolide) (PGA-PCL) at gradient ratios. MBG/PGA-PCL (PGC/M) scaffolds with MBG incorporation ratio at 0, 10%, 25% and 40% (PGC/M0-40) were synthesized using a modified solvent casting-particulate leaching method, and their physiochemical and biological properties were comprehensively evaluated. PGC/M scaffolds exhibited highly perforated porous structure with a large-pore size of 300–450 μm , with ordered MBGs of around 6.0 nm mesopores size uniformly dispersed. The increase in MBG incorporation ratio significantly improved the scaffold surface hydrophilicity, apatite-formation ability and pH stability, increased the weight loss rate while insignificantly influenced the molecular chains degradation of PGA-PCL component, and facilitated the attachment, spreading, viability and proliferation of rat bone marrow stromal cells (rBMSCs) on scaffolds. Moreover, rBMSCs cultured on PGC/M10-40 scaffolds demonstrated enhanced ALP activity and osteogenesis-related gene expression in a MBG dose-dependent manner as compared with those cultured on PGC/M0 scaffolds. When implanted to the rat cranial bone defect, PGC/M25 and PGC/M40 scaffolds induced significantly better bone repair as compared to PGC/M0 and PGC/M10 scaffolds. Besides, the biodegradability of PGC/M scaffolds correlated with the MBG incorporation ratio. These data suggested this novel PGC/M scaffolds as promising bone repair biomaterial with highly tunable hydrophilicity, bioactivity, cytocompatibility, osteogenic activity as well as biodegradability.

1. Introduction

Bone defects reaching critical size require medical interventions to facilitate full recovery [1,2]. One common clinical intervention is to graft the defect region with scaffolds that support cell migration, proliferation and osteogenic differentiation [3,4]. Artificial scaffolds circumvent the donor site scarcity and complications associated with autografts and the immunogenic and pathogenic risks associated with allografts or xenografts [5], but the physiochemical and biological

performance of currently available scaffolds needs further polish.

Synthetic biodegradable polyesters, such as polycaprolactone (PCL), polyglycolide (PGA), polylactide (PLA) and their copolymers poly(lactide-co-glycolide) (PLGA), are of superior biocompatibility, controllable degradability, high processability, and thus have been widely used to construct bone tissue engineering scaffolds [6,7]. Ideally, the pace of biodegradation and new bone formation should be synchronized during the restitution process after scaffold implantation, but this feature currently has not been satisfactorily achieved on

Peer review under responsibility of KeAi Communications Co., Ltd.

* Corresponding author. No.24, South Section 1, 1st Ring Road, Chengdu, 610065, PR China.

** Corresponding author. No.14, Ren Min Nan Road, Chengdu, 610041, PR China.

E-mail addresses: lijingtao86@163.com (J. Li), nic0700@scu.edu.cn (G. Yin).

¹ These authors contributed equally.

<https://doi.org/10.1016/j.bioactmat.2021.11.034>

Received 31 August 2021; Received in revised form 5 November 2021; Accepted 16 November 2021

Available online 21 December 2021

2452-199X/© 2021 The Authors. Publishing services by Elsevier B.V. on behalf of KeAi Communications Co. Ltd. This is an open access article under the CC BY-NC-ND license (<http://creativecommons.org/licenses/by-nc-nd/4.0/>).

polymer-based scaffolds.

PGA is the only hydrophilic biodegradable polymer and possesses the highest degradation rate among synthetic biodegradable polyesters [8, 9]. PCL is semicrystalline polymer and degrades slowly because of the high hydrophobicity of ϵ -caprolactone [8,9]. We previously synthesized bi-block PGA-PCL polymers and found that a broad range of in vivo degradation pace could be achieved by tuning the feed composition of the two components. The bi-block PGA-PCL material with a 30/70 (PGA/PCL) ratio exhibited a degradation rate close to the pace of new bone formation [1] and was fabricated into three-dimensional scaffolds with expected pore morphology and porosity using solvent casting-particulate leaching method.

The PGA-PCL polymers themselves, however, are of low hydrophilicity, bioactivity, and osteoinductivity [10–14]. Additionally, the acidic degradation of polymers release byproducts that decrease the local pH value and induce overly inflammatory response [15–17]. To counteract these drawbacks, bioactive inorganic components, such as hydroxyapatite (HAp) [18,19], calcium phosphate (CaP) [2,20], β -tricalcium phosphate (β -TCP) [14,21,22] or bioactive glass (BG) [2,23,24], have been incorporated into polymers to develop inorganic/organic composites, aiming to improve the hydrophilicity and bioactivity, stabilize the surrounding pH and enhance osteogenic capacity.

The increase in surface area and pore volume of biomaterials has been associated with accelerated apatite deposition and enhanced osteogenic bioactivity [25,26]. Mesoporous bioactive glass (MBG) particles of CaO–SiO₂–P₂O₅ composition present increased surface area and nanopore volume and exhibit superior bioactivity versus the non-mesoporous BG [25,27,28]. Although numerous studies have confirmed that incorporation of MBG improves the osteogenic capacity of polymer-based composites [10–12,29–31], further investigation is still required on fine-tuning the degradation-bone formation pace balance in this material system.

In this study, we constructed MBG/PGA-PCL composite scaffolds for the first time and comprehensively assessed the effect of MBG incorporation ratio on the physiochemical and biological properties of the scaffolds.

2. Materials and methods

2.1. Chemicals and reagents

Poly(ethyleneglycol)-block-poly(propyleneglycol)-block-poly(ethyleneglycol) (EO20-PO70-EO20, P123, M_w = 5800, AR) was purchased from Sigma-Aldrich, Saint Louis, USA. Tetraethyl orthosilicate (TEOS, AR), triethyl phosphate (TEP, AR), calcium nitrate tetrahydrate (Ca(NO₃)₂·4H₂O, AR), and hydrochloric acid (HCl, AR) were purchased from Kelong, Chengdu, China. Double deionized water (DDW) was used as solvent and for washing. PGA-PCL was supplied by Medical Device Research Institute, Shandong, China. Hexafluoroisopropanol (HFIP) was purchased from Aladdin, Shanghai, China.

2.2. Preparation of MBG

MBG was prepared according to the previous report [31] with modifications. The MBG powder was composed of SiO₂, CaO and P₂O₅, in which the molar percentage of Si, Ca and P was 57.2%, 35.3% and 7.5%, respectively. In a typical synthesis, 1.0 g of Pluronic P123 was dissolved in 50 mL of 2 mol/L HCl while stirring at 37 °C in a water bath. After completely dissolution, 1.98 g of Ca(NO₃)₂·4H₂O, 0.3301 g of TEP and 2.833 g of TEOS were added in sequence, in which the drop speed of TEP and TEOS was 20 drops per minute for the more complete hydrolysis of TEP and TEOS. The mixture was stirred at room temperature for 24 h, transferred into a PTFE bottle and hydrothermally treated at 100 °C for 48 h. The resultant precipitates were collected through filtration, washed with DDW, dried at 60 °C overnight and then calcined in air at 700 °C for 6 h to remove the templates. Finally, the obtained

MBG was finally ground and sieved through 325 mesh.

2.3. Preparation of MBG/PGA-PCL (PGC/M) composite porous scaffolds and films

The MBG/PGA-PCL composite scaffolds were prepared by a modified solvent casting-particulate leaching method using sodium chloride (NaCl) particles as porogen. The compositions of different PGC/M scaffolds were listed in Table 1. The selection for these gradient MBG addition ratios was to investigate the effect of the significantly increased MBG contents in scaffolds on structural performances and osteogenic effects of scaffolds on basis of the preliminary experimental results of preparation. The ratio of the PGA-PCL to HFIP was fixed at 10% (w/v). 1 g PGA-PCL was dispersed in 10 mL HFIP and continuously stirred until complete PGA-PCL dissolution. Various amount of MBG powder was added into the solution, continuously stirred for 12 h and sonicated for 30 min to disperse the glass powders uniformly. The mass ratio of porogen to PGA-PCL was 6/1 (w/w). NaCl particles of 300–450 μ m diameter were added into the suspension and continuously stirred for 15 min. The suspension solution was then slowly dropped into ethanol solvent while stirring. Small PGC/M composite particles would separate from the mixture solvent since ethanol diffused into HFIP. The PGC/M precipitates were continuously washed in ethanol under stirring for 3 h to further remove HFIP. Then, the PGC/M precipitates were loaded into a stainless-steel mold of 6 mm diameter and pressed at 10 MPa for 5 min under room temperature to obtain a 15 mm high cylindrical specimen. The samples were air-dried under flowing air for 24 h to further remove remaining solvent. The specimens were then immersed in DDW for 72 h under stirring and the water was replaced approximately every 6 h to leach out the salt particulates. Finally, the samples were air-dried in the room temperature and cut into slices for subsequent use.

The PGC/M composite films were prepared similarly without adding NaCl porogens. The MBG/PGA-PCL suspension was casted on a Teflon mold, air-dried for 24 h and vacuum dried overnight to remove the remaining solvent. The films were cut into appropriate size for subsequent use.

2.4. Morphological characterization of MBG powders and PGC/M porous scaffolds

The morphology of MBG particles was examined by a scanning electron microscope (SEM, S-4800, Hitachi, Japan). The phase composition and the ordered degree of MBG mesopores were assessed using an X-ray diffractometer (XRD, EMPYREAN, PANalytical B.V., Netherlands) equipped with Cu K α radiation (wavelength 1.5418 Å). Small-angle X-ray diffraction (SAXRD) patterns were collected in the 2 θ range between 0.5 and 8° with a step size of 0.01313° and a counting time of 148.92 ms per step. Wide-angle XRD (WAXRD) patterns were captured in the 2 θ range between 10 and 80° with a scan speed of 5°/min. The morphology of mesoporous structures was analyzed with a transmission electron microscope (TEM, Tecnai G2 F20 S-TWIN, FEI, USA). The surface area was determined by applying the Brunauer–Emmett–Teller (BET) method with N₂ adsorption–desorption isotherms. The distribution of pore size and the pore volume were calculated by the Barrett–Joyner–Halenda (BJH) model from the adsorption branch of the isotherm with a porosimeter (Kubo X1000, BEIJING Builder Electronic Technology CO., LTD, China). Moreover, the morphology of PGC/M scaffolds was observed by

Table 1
Ingredients of different PGC/M scaffolds.

Group	MBG/(PGA-PCL + MBG) (w/w, %)	PGA-PCL (w, g)	MBG (w, g)
PGC/M0	0	1.0	0.00
PGC/M10	10	1.0	0.12
PGC/M25	25	1.0	0.34
PGC/M40	40	1.0	0.67

a SEM, and the PGC/M scaffolds were scanned by a high-resolution Micro-CT Systems (VivaCT 80, SCANCO Medical AG, Switzerland) to analyze their porosity.

2.5. Inorganic element assessment

The contents of Si, Ca and P elements in dried MBG powders were measured by X-ray fluorescence spectrometer (XRF, XRF-1800, SHIMADZU, Japan). The distribution of Si, Ca and P elements in PGC/M scaffolds was measured with an energy dispersive X-ray spectrometer (EDS, INCA Energy, Oxford Instruments, UK).

2.6. Surface wettability evaluation

The surface wettability was determined by measuring the dynamic water contact angle on a Contact Angle Meter (JC2000C1, Shanghai Zhongchen Digital Technology Apparatus Co., Ltd, China). Distilled water dropping onto the films and scaffolds was photographed continuously at every 20s. The contact angle of the drops was calculated following the software manual. Two independent quintuplicate experiments were performed to record the mean value.

2.7. Degradation, iron release and biological activity of PGC/M porous scaffolds

PGC/M scaffolds were weighed (M_0) and immersed in sterile PBS under oscillating condition at 37 ± 0.5 °C. The ratio of the solution volume to the scaffold mass was 100 mL/g. The scaffolds were taken out at 1, 4, 7, 10, 14, 21 and 28 days after immersion, gently washed with deionized water, dried at room temperature and weighted (M_t). The degradation ratio of scaffold weight was calculated by the following equation:

$$WC (\%) = ((M_0 - M_t) / M_0) \times 100 \%$$

The molecular weight (M_w) of the PGA-PCL at 0, 7, 14, 21 and 28 days after immersion was measured by Gel Permeation Chromatography (GPC, HLC-8320GPC, TOSOH, Japan). The concentrations of Si and Ca ions released from PGC/M scaffolds were determined by inductive coupled plasma atomic emission spectrometry (ICP-OES, Spectro Arcos, Germany), and the pH values were detected by a pH meter (PHS-3E, INESA, China) at the predetermined time points. The surface morphology and composition of the scaffolds after soaking in the PBS were characterized by SEM and EDS. The phase composition of substances formed on the surface of scaffolds was examined by WXR D at 0, 1 and 28 days after immersion.

2.8. Isolation and identification of rat bone marrow stromal cells (rBMSCs)

rBMSCs were isolated from the femurs and tibias of male SD rats weighting 100–120 g as described previously [32]. Cell were cultured in α -MEM medium supplemented with 10% fetal bovine serum (Gibco). The third passage was used for analyses. Surface markers of rBMSC were examined using flow cytometry according to the procedures. The attached rBMSCs were digested with trypsin, centrifuged, washed twice with PBS solution to prepare single-cell suspension at the density of 1×10^7 cells/ml. 100 μ l of cells suspension was incubated with (PE)-conjugated monoclonal antibody against CD29 (1:100 dilution) and CD90 (1:100 dilution), (FITC)-conjugated monoclonal antibody against CD34 (1:100 dilution) and CD45 (1:100 dilution) and corresponding isotype controls (all antibodies were purchased from BD Biosciences) for 30 min at room temperature in dark. Flow cytometry was performed on FACS-Calibur (BD Biosciences, San Diego, USA). The data were analyzed with the Flowjo software (Flowjo, USA).

2.9. Analyses of rBMSCs on PGC/M scaffolds

The scaffolds prepared for biological assays were immersed in 75% ethanol for 30 min and radiated under ultraviolet light for 60 min with periodical rotation. rBMSCs were seeded on the scaffolds at a concentration of 2.0×10^4 cells/well and incubated at 37 °C in humidified 5% CO₂ atmosphere.

After incubation for 3 days, the cells/scaffolds were rinsed with PBS, fixed in 4% paraformaldehyde for 30 min, permeabilized with 0.1% Triton X-100 for 10 min, and rinsed twice in PBS. Samples were immersed in 1% bovine serum albumin (BSA) in PBS for 20 min to block nonspecific bindings and incubated with diluted phalloidin (Thermo Fisher, USA) to stain actin filaments of microkeleton and 4'-6-diamino-2'-phenylindole dihydrochloride (DAPI, Solarbio, China) to stain nuclei. The samples were then observed under a fluorescence microscope confocal laser scanning microscope (LSM 880, Zeiss, Germany).

The morphological characteristics of the cells attached to the scaffolds were assessed using SEM. After 3 days of coculture, the samples were fixed with 4% glutaraldehyde for 2 h, washed three times with PBS and sequentially dehydrated in gradient ethanol (30%, 50%, 70%, 85%, 90%, 95%, 100%). The samples were dried by carbon dioxide for 1 h before coating with gold for SEM examination.

Cell proliferation was evaluated using MTT assay. The cells were seeded on the scaffolds at a density of 1.0×10^4 /well. After coculture for 24 h, the samples were transferred to another 48 well plates. 200 μ l PBS and 20 μ l MTT solution (5 mg ml⁻¹) was added into each well and incubated at 37 °C for 4 h to form formazan crystals. After removal of the MTT solution, 150 μ l dimethyl sulfoxide (DMSO) was added followed by shaking for 10 min to completely dissolve the formazan crystals. 100 μ l supernatant was transferred to 96 well plate for detection. The absorbance was quantified spectrophotometrically at wavelengths of 490 nm using a microplate reader (Tunable VERSA max, Molecular Devices, USA). The modified OD values were normalized to those of the PGC/M0 group.

The cell viability was analyzed using a Live/Dead cell kit (CA1630, Solarbio, China). Briefly, after a 72 h coculture, cell/scaffolds were stained with 300 μ l of combination dye for 10 min according to the manufacturer's protocol and observed under a Fluorescence inverted microscope (TE2000-S, OLYMPUS, Japan).

2.10. Osteogenic differentiation of rBMSCs on scaffolds

The rBMSCs were seeded onto the sterilized scaffolds at a density of 2.0×10^4 cells/well and coculture for 7 days before ALP activity assay and ALP staining. The attached cells were trypsinized and transferred into new plates for subsequent 24 h spreading. Then, the cells were lysed with 0.1% Triton X-100 for 10 min and the cell lysate was used to measure ALP activity by an ALP microplate test kit (Nanjing Jiancheng Bioengineering Institute, Nanjing, China). The quantity of ALP was measured at 520 nm using a microplate reader. The reads were normalized by the total protein content determined by BCA protein assay kit (Nanjing Jiancheng Bioengineering Institute, Nanjing, China). ALP staining of the cells on scaffolds was performed using BCIP/NBT Alkaline Phosphatase Color Development Kit (Beyotime, China). After fixation with 2.5% glutaraldehyde, the cells/scaffolds were incubated in a mixture of nitro-blue tetrazolium and 5-bromo-4-chloro-3-indolyl-phosphate and observed with a digital camera.

The mRNA expression of several osteogenic genes, including bone morphogenetic protein 2 (*Bmp-2*), runt-related transcription factor 2 (*Runx-2*), vascular endothelial growth factor (*Vegf*), collagen type I (*Col I*), osteopontin (*Opn*), bone sialoprotein (*Bsp*) and fibroblast growth factor (*Fgf2*), were quantitatively determined by real-time polymerase chain reaction (RT-qPCR). The primers used were provided in Table S1. After 7 and 14 days of coculture, total RNA was collected from cells grown on the scaffolds using the TRIzol reagent (Ambion, Grand Island, NY, USA). The reverse transcription was performed using a Thermo

scientific RevertAid First Strand CDNA Synthesis Kit K1622 (Thermo scientific, MA, USA) in T100™ Thermal Cycler (Bio-rad, CA, USA). Quantitative real-time PCR was performed on an CFX Connect™ Optics Module (Bio-rad, CA, USA) using the iQ™ SYBR® Green Supermix (Bio-rad). The mRNA copy numbers were calculated for each sample by using the cycle threshold (Ct) value, and GAPDH was amplified in parallel with the tested genes. The number of amplifications steps required to reach an arbitrary Ct was computed. The relative gene expression was represented by $2^{-\Delta(\Delta Ct)}$, where $\Delta(\Delta Ct) = \Delta Ct_{\text{target gene}} - \Delta Ct_{\text{GAPDH}}$. The fold change for the treatment was defined as the relative expression compared with control GAPDH expression, calculated as $2^{-\Delta(\Delta Ct)}$, where $\Delta(\Delta Ct) = \Delta Ct_{\text{experiment}} - \Delta Ct_{\text{control}}$. All experiments were conducted in triplicate.

2.11. In vivo degradation of PGC/M scaffolds

The in vivo degradation of PGC/M scaffolds was evaluated using a rat intramuscular implantation model. Four-week-old male SD rats were obtained from Chengdu Dossy Experimental Animals CO.,LTD, and all animal experiments were approved by the Animal Ethics Committee of Sichuan University, People's Republic of China. The rats were anesthetized with 1% sodium pentobarbital (50 mg/kg body weight). The scaffolds ($\varnothing 6 \times 2$ mm) were implanted into the back muscles on both sides. The rats were sacrificed to harvest the residual implants at 4, 8 and 12 weeks after implantation. The harvested samples were fixed in 4% paraformaldehyde, dehydrated in gradient alcohol, embedded in paraffin, sectioned at 5 μm and stained with Hematoxylin and eosin (H&E) for histological evaluation.

2.12. Implantation of PGC/M scaffolds to rat calvarial bone defects

The rat calvarial defect model was used to investigate the in vivo osteogenic capacity of the various PGC/M scaffolds. Four-week-old male C57 mice were obtained from Chengdu Dossy Experimental Animals CO.,LTD. After adaptation for one week, 14–20 g mice were anesthetized with a 1% sodium pentobarbital (50 mg/kg body weight). The head skin was sterilized with 75% ethanol and betadine and a sagittal incision of 0.5 cm was made with surgical blade to expose the calvarium. Two critical-sized defects were created on the left and right calvarial bones using a 4-mm-diameter circular drill. The defected were rinsed with saline solution and grafted scaffolds ($\varnothing 4 \times 2$ mm): PGC/M0 (n = 9), PGC/M10 (n = 9), PGC/M25 (n = 9), and PGC/M40 (n = 9).

The in vivo bone ingrowth of the implanted scaffolds was evaluated by Micro-CT measurements. After 4 weeks or 8 weeks implantation, the skull bones were harvested and fixed with 4% paraformaldehyde for 24 h at room temperature. Synchrotron radiation microcomputed tomography (SRmCT) measurements were performed on the harvested samples at a high-resolution Micro-CT Systems (VivaCT 80, SCANCO Medical AG, Switzerland). Scanning was performed at 70 kV and 114 μA with a thickness of 0.015 mm per slice in medium-resolution mode, and 200 ms integration time. VG Studio software (Volume Graphics, Germany) was served for the visualization of the reconstructed 3D images and the percentage of new bone volume relative to tissue volume (BV/TV), trabecular thickness (Tb.Th) and trabecular number (Tb.N) in the bone defect were calculated using the Scanco analysis software.

The skulls at week 8 time point were fixed with 4% paraformaldehyde at room temperature for 24 h, decalcified in 10% EDTA for 1 week, dehydrated in gradient ethanol, embedded in paraffin and sectioned at 5 μm of thickness for Hematoxylin and eosin (H&E) staining and Masson's Trichrome staining.

2.13. Statistical analysis

All data were presented as mean \pm standard deviation (SD). Statistical analysis was performed by one-way ANOVA using SPSS software. The methods of post-hoc tests after one-way ANOVA were LSD (Least

Significance Difference) and S–N–K (Student-Newman-Keuls). A statistical significance was accepted at $p < 0.05$.

3. Results

3.1. Characterization of MBG powders

SEM images revealed the worm-like morphology of individual MBG particle (Fig. 1A). WXR patterns of MBG powder displayed no remarkable diffraction peaks except for broad SiO_2 at $2\theta = 15\text{--}35^\circ$ (Fig. 1B), indicating that MBG particles existed in the form of amorphous phase [28]. SXRD patterns exhibited an apparent diffraction peak at around $2\theta = 1.05\text{--}1.19^\circ$ due to $d_{(100)}$ reflection of MBG hexagonal space group $p6mm$, and two other weak diffraction peaks at $2\theta = 1.8\text{--}2.3^\circ$ resulted by $d_{(110)}$ and $d_{(200)}$ reflections (Fig. 1C), indicating that MBG had an high long-rang ordered mesoporous structure [28]. N_2 adsorption–desorption isotherms of MBG showed a type IV isotherm pattern with H1 type hysteresis loops (Fig. 1D) which was typical to mesoporous materials [33]. The diameter of MBG mesopore was mainly distributed around 6.12 nm (Fig. 1E). The mesoporous structure of MBG was intuitively observed with TEM as shown in Fig. 1F. The ordered pore arrangement of MBG at [100] direction and highly ordered mesoporous hexagonal structure were clearly visible, which was consistent with the N_2 adsorption-desorption and the SXRD results. The detailed MBG textural parameters were listed in Table 2 and the MBG compositions were also analyzed by XRF (Table S2).

3.2. Characterization of PGC/M porous scaffolds

The porosity of pure PGA-PCL (PGC/M0) scaffolds prepared with different feed ratio of porogens was measured. When the mass ratio of PGA-PCL/NaCl porogens was 1:6, the scaffold porosity was $80.92 \pm 5.65\%$ (Fig. S1A) which met the porosity requirement of bone tissue-engineering [3,4]. Micro-CT scanning of the PGC/M0 scaffold revealed evenly distributed perforated pores in both the internal and external area of the scaffold with about 75% calculated porosity, which was consistent with the experimental porosity (Fig. S1 A, B).

The SEM results showed that all PGC/M scaffolds maintained a highly perforated porous structure (Fig. 2A), and the large-pore size of PGC/M0, PGC/M10, PGC/M25 and PGC/M40 scaffolds was $395 \pm 22 \mu\text{m}$, $387 \pm 19 \mu\text{m}$, $378 \pm 19 \mu\text{m}$ and $364 \pm 29 \mu\text{m}$, respectively (Table S3). The porosity of PGC/M0–40 scaffolds was successively $75.9 \pm 3.2\%$, $72.7 \pm 2.0\%$, $70.5 \pm 1.1\%$ and $68.8 \pm 1.6\%$ (Fig. 2C), as measured by Micro-CT method. Moreover, some pores slightly collapsed with the increase in MBG ratio, which was mainly attributed to the breakage of continuous organic PGA-PCL phases due to MBG incorporation, but the interconnective large-pore structure was still maintained. In addition, the pore structure collapsed more seriously when MBG addition ratio was over 40%, therefore, the highest MBG incorporation ratio remained at 40% to maintain the integral structure of scaffolds. Particles with diameter less than 10 μm attaching to the inner wall of scaffolds were clearly shown by SEM scanning and their number increased along with the increase in MBG ratio (Fig. 2A).

Element mapping analysis demonstrated that Si, Ca, P elements were uniformly distributed in the pores PGC/M scaffolds and their contents significantly increased as the MBG ratio increased (Fig. 2B). This was further verified by the significantly increased mean point density of Si, Ca, P elements (Fig. 2D) and the continuously enhanced intensity of EDS peaks (Fig. S2). These results confirmed that the particles observed under SEM were MBG particles.

3.3. Surface wettability of PGC/M films and scaffolds

For pristine PGC films, the water contact angle (WCA) reached up to $66.10 \pm 1.40^\circ$ in 180 s from an initial value of $69.75 \pm 1.89^\circ$ (Fig. 3A). For PGC/M10, PGC/M25 and PGC/M40, the initial WCA decreased by

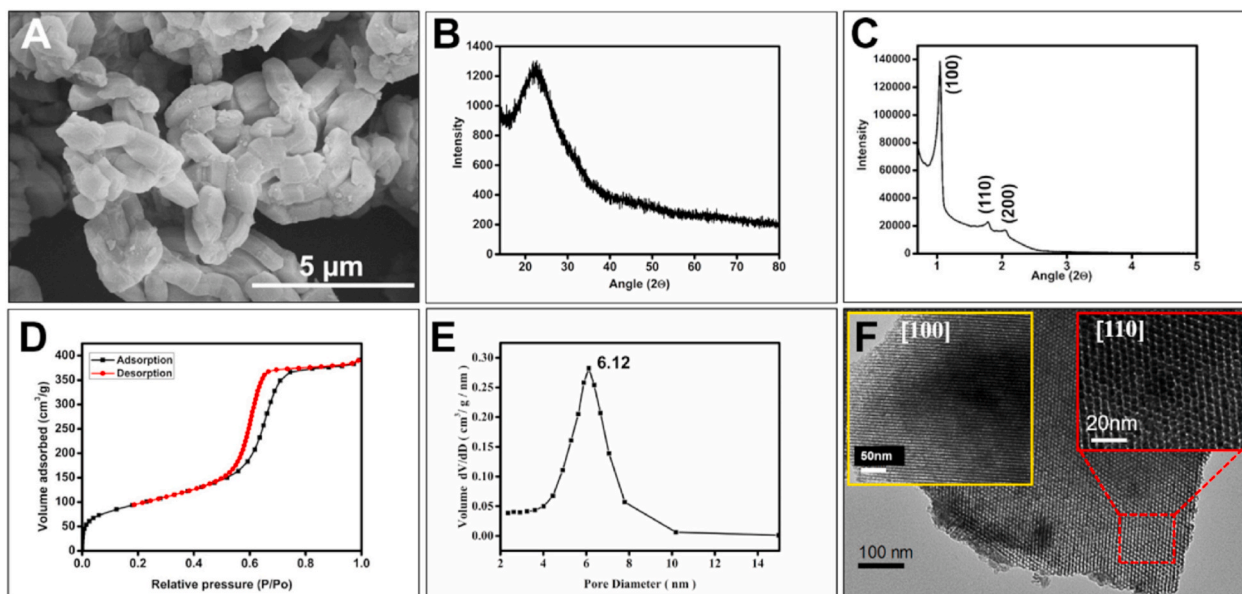


Fig. 1. Characterization results of structural features of MBG particles. (A) SEM images of MBG particles. (B) Wide-angle XRD patterns of MBG particles. (C) Small-angle XRD patterns of MBG particles. (D) N_2 adsorption–desorption isotherms of MBG particles. (E) Distribution of mesoporous pore diameter of MBG particles. (F) TEM analysis for the MBG particles.

Table 2
Structural parameters of the MBG particles.

Group	S_{BET} ($m^2 g^{-1}$)	D_p (nm)	V_p ($cm^3 g^{-1}$)	V_m ($cm^3 g^{-1}$)
MBG	348	6.12	0.61	0.15

Specific surface area, diameter of pore, pore volume and micropore volume were abbreviated to S_{BET} , D_p , V_p and V_m , respectively.

about 9° , 19° and 24° , and the final WCA reached $57.88 \pm 1.24^\circ$, $45 \pm 5.6^\circ$ and $32 \pm 9.9^\circ$ respectively. The comparison between 0 and 60 s showed that the WCA of PGC/M films significantly decreased with the increase of MBG ratio ($p < 0.05$), indicating that MBG would further enhance wettability of PGC films [34]. The porous scaffolds exhibited WCA variation similar to PGC/M films (Figs. 3C and 4D). For pristine porous PGC scaffold, the WCA was initially $76.03 \pm 6.6^\circ$ and reached $69.32 \pm 2.79^\circ$ in 80 s (Fig. 3C). After incorporation of MBG, the initial WCA decreased to $67.42 \pm 4.48^\circ$, $69.50 \pm 1.84^\circ$, $69.51 \pm 0.64^\circ$ for PGC/M10, PGC/M25 and PGC/M40 scaffold respectively, but no significant difference was observed among the three groups, suggesting that porous structure exerted an impact on wettability. The final WCA, however, reached $61.32 \pm 4.84^\circ$, $59.70 \pm 0.21^\circ$, $54.60 \pm 6.87^\circ$ for the PGC/M10-40 scaffold after 80 s, suggesting a significant decline compare to the PGC/M0 scaffold ($p < 0.05$). Moreover, the WCA of PGC/M25 and PGC/M40 scaffolds at 60 s exhibited a marked decrease in contrast to the PGC scaffold ($p < 0.05$).

3.4. *In vitro* and *in vivo* degradation of PGC/M scaffolds

All scaffolds maintained relatively intact morphology with some loss of volume after 4 weeks immersion in PBS (Fig. 4A). The weight loss rate of all scaffolds gradually increased with the immersed time, and the weight loss rate was higher in PGC/M10-40 groups than that in PGC/M0 group (Fig. 4B). The weight-average molecular weight (M_w) of the PGA-PCL component decreased in all scaffolds with the fastest decrease observed in the first week. The PGA-PCL M_w in PGC/M10-40 scaffolds was similar to that in PGC/M0 at all time points, indicating that MBG incorporation exerted no significant impact on the degradation of PGA-PCL molecular chains (Fig. 4C). The pH values of the immersion solution in all groups were above 7.2 during the 4 weeks. The pH values in the

PGC/M10-40 groups were higher than in the PGC/M0 group, and the highest pH values were recorded in the PGC/M40 group at all time points (Fig. 4D).

In vivo degradation was evaluated by implanting the scaffolds into rat back muscle for 4, 8 and 12 weeks. At 4 weeks after implantation, the majority of the space within the polymer in PGC/M25 and PGC/M40 scaffolds were filled with fibrous tissues, indicating improved histocompatibility with MBG incorporation (Fig. 5). Remnant materials were clearly observed in each group (red arrows). After 8 weeks, more fibrous tissues grew into scaffolds and the signs of degradation became more evident. Furthermore, the amounts of remnant materials decreased with the increase of MBG contents (Fig. 5). After 12 weeks, vascularization was also observed in materials (black arrows). The degraded trend of scaffolds at 12 weeks was similar to those at 8 weeks. Some remnant scaffolds materials still could be observed in PGC/M25 and PGC/M40 groups, indicating that the complete degradation of the implanted scaffolds required a longer time *in vivo* of rats. Comparison in the remnant material among groups showed that the increase in MBG incorporation ratio was correlated with accelerated scaffolds degradation. Moreover, a decreased inflammation in PGC/M10-40 groups could be observed with the time.

3.5. Ions release and bioactivity of PGC/M scaffolds

The Ca and Si ions release was measured after soaking scaffolds in PBS. The release of Ca ions decreased progressively with the most release observed in the first week. Samples with higher ratio of MBG incorporation demonstrated slower release (Fig. 6A). In contrast, the Si ions release gradually increased over time, and faster release was observed in samples with higher MBG ratio (Fig. 6B).

The surface morphology of scaffolds after PBS immersion was shown in Fig. 7A. A layer of particles with lamellar shape formed on the surface of PGC/M10-40 scaffolds and the amounts of those particles significantly increased with the increase in both MBG ratio and the soaking duration. No particles deposition was observed on the surface of PGC/M0 scaffold during the entire soaking period.

Particles on the surface of PGC/M40 scaffold at 28 days were analyzed by EDS and revealed a Ca/P ratio of 1.67 which was close to hydroxyapatite (Fig. 7B). To further determine the phase composition of

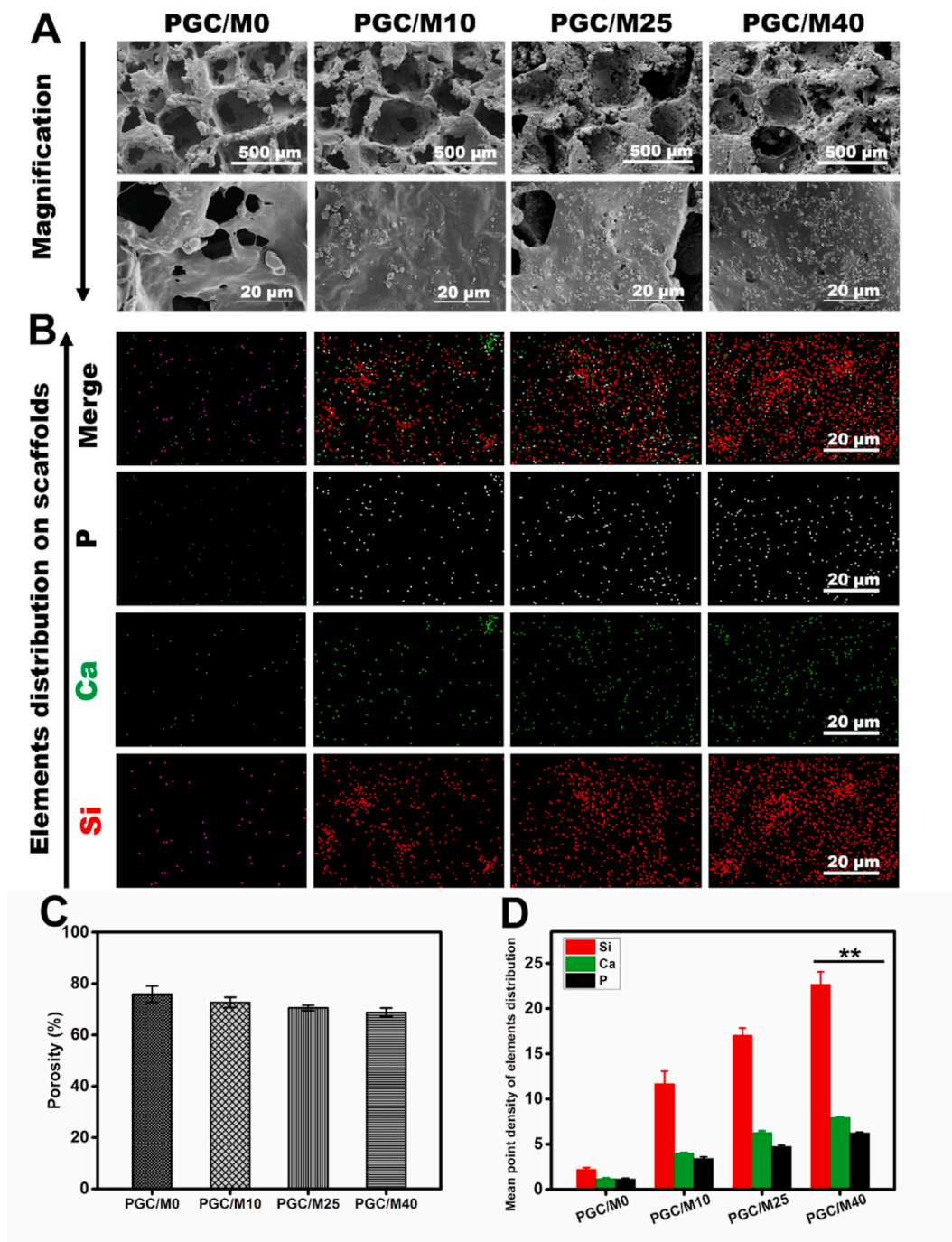


Fig. 2. Morphology features and active element distribution of MBG/PGA-PCL scaffolds. (A) SEM of the scaffolds. (B) EDS elemental mapping of a randomly selected area on scaffolds. (C) Porosity of PGC/M scaffolds via Micro-CT calculation. (D) Quantitative statistics of different elements distribution on scaffolds (Mean point density of every element on three randomly selected area of scaffolds was measured by Image J software) ** $p < 0.01$, PGC/M40 group VS. the PGC/M10 and PGC/M25 groups.

particles, the surface particles on PGC/M scaffolds were investigated by XRD. The characteristic peaks of hydroxyapatite were observed in the XRD patterns of all PGC/M10-40 surface particles, and these peaks were stronger at 28 days than at 1 day after immersion (Fig. 7C(b-d)). In contrast, XRD patterns of surface particles on PGC/M0 scaffold (Fig. 7C(a)) or unsoaked PGC/M scaffolds (Fig. 7C(a-d)) showed no characteristic peaks of hydroxyapatite. These results confirmed that the particles on the surface of PGC/M scaffolds were hydroxyapatite, and also suggested that the incorporated MBG promoted the hydroxyapatite formation and improved the bioactivity of PGC/M scaffolds.

3.6. Cytocompatibility of PGC/M scaffolds

The primary cells isolated from rat long bones were identified as rBMSCs by their long fusiform morphology and CD29⁺ CD90⁺ CD34⁻ CD45⁻ surface marker expression (Fig. S3). Cells on PGC/M25 and M40 scaffolds exhibited higher proliferation rates than on PGC/M0 and PGC/M10 scaffolds at 24 h ($p < 0.05$) (Fig. 8A). rBMSCs exhibited good cell viability on all scaffolds with negligible number of dead cells (Fig. 8B). The number of live cells on scaffolds surface significantly increased with the increase in MBG ratio (Fig. 8B and C). The more MBG incorporated into PGC/M scaffolds, the more cells

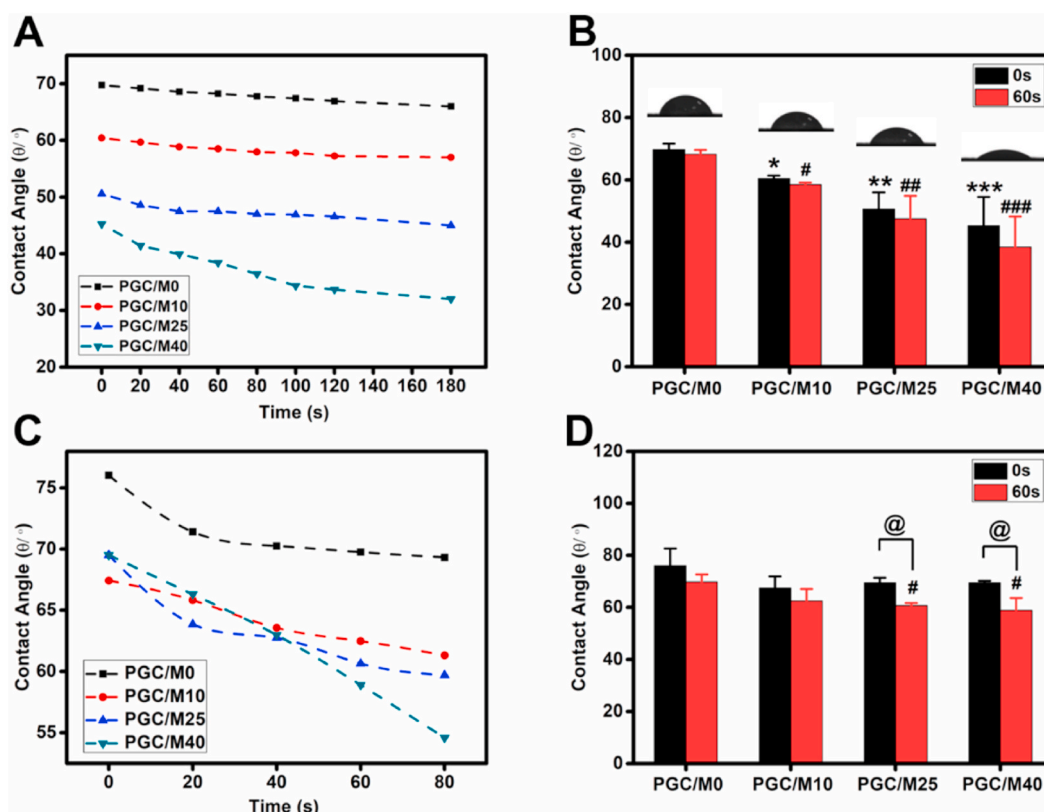


Fig. 3. Changed contact Angle of PGC/M membrane materials and porous scaffolds. (A) and (C) shows the time-dependent changes in the advancing contact angle for PGC/M mats and scaffolds, respectively. The symbols indicate average data points at every 20 s. (B) and (D) compares the water contact angle between 0 and 60s for PGC/M mats and scaffolds, respectively. (n = 10). *p < 0.05, **p < 0.01, ***p < 0.001 VS. the PGC/M0 group at 0 s; #p < 0.05, ##p < 0.01, ###p < 0.001 VS. the PGC/M0 group at 60s. @p < 0.05 VS. the relative PGC/M25 or PGC/M40 group between 0 and 60s.

grown on scaffolds. rBMSCs on PGC/M25 and PGC/M40 scaffolds displayed multilayered, clustered and confluent morphology with more actin filaments linking adjacent cells, while those on PGC/M0 and PGC/M10 scaffolds exhibited monolayered and dispersed morphology with fewer actin filaments and poor spreading (Fig. 8C). Besides, the attachment and morphology of rBMSCs grown on all scaffolds could be clearly observed by SEM (Fig. 8C, the red arrow).

3.7. Osteogenic capacity of PGC/M scaffolds

rBMSCs demonstrated upregulated expression in Bmp-2 and Runx2 when cultured on PGC/M25-40 scaffolds for 7 days and on PGC/M10-40 scaffold for 14 days as compared to those on PGC/M0 ($p < 0.05$) (Fig. 9A and B). The extent of upregulation correlated with the MBG incorporation ratio. Furthermore, expressions of Bmp-2 in PGC/M25-40 groups ($p < 0.05$) and Runx2 in PGC/M40 group ($p < 0.001$) at day 14 were significantly lower than at day 7. The expression level of Vegf in PGC/M40 group at day 7 and PGC/M25-40 groups at day 14 was significant higher than that in PGC/M0 group ($p < 0.05$) (Fig. 9C). The expression level of Fgf and Col-I exhibited a significant increase in PGC/M25 and PGC/M40 groups at day 14 compared to the PGC/M0 group at day 14 ($p < 0.05$) or the corresponding PGC/M25 and PGC/M40 groups at day 7 ($p < 0.05$) (Fig. 9D and E). The expression levels of Opn was significantly higher in PGC/M25-40 groups than PGC/M0 group at both day 7 and 14 ($p < 0.05$) (Fig. 9F). Furthermore, the expression level of Opn gene expression in PGC/M40 group was evidently higher at day 14 than that at day 7 ($p < 0.01$). Compared to the PGC/M0 group, the expression level of Bsp was significant higher in PGC/M40 group at day 7 ($p < 0.05$) and in PGC/M10-40 groups at 14 day ($p < 0.05$) (Fig. 9G). Besides, the Bsp expression level in PGC/M40 group was further significantly elevated from 7 to 14 day ($p < 0.05$). Both the intensity of ALP staining

and ALP activity on the PGC/M25 and PGC/M40 scaffolds was considerably stronger than that on the PGC/M0 and PGC/M10 scaffolds (Fig. 9H).

3.8. Grafting rat calvarial bone defect with PGC/M scaffolds

The PGC/M0-4 scaffolds were implanted to the rat calvarial critical-size defect and evaluated at 4 and 8 weeks. All the implanted scaffolds maintained relatively intact morphology with limited edge degradation at weeks 4, and more capillaries was observed on the surface of PGC/M 25–40 than on PGC/M0-10 scaffolds (Fig. 10A, left). At 8 weeks, the remnant size of the scaffolds was significantly smaller with higher MBG incorporation ratio (Fig. 10A, right), which was consistent with the degradation trend observed in the rat back muscle implantation model (Fig. 5).

Micro-CT scanning showed very limited bone repair in the PGC/M0 group but evident new bone ingrowth extending from the defect edge in the PGC/M10-40 group both at weeks 4 and 8. The amount of new bone formation was higher in groups with higher MBG incorporation ratios (Fig. 10A). The bone volume/total volume (BV/TV), trabecular thickness (Tb.Th) and trabecular number (Tb.N) in the defect region in PGC/M25-40 groups were significantly higher than in PGC/M0-10 groups both at weeks 4 ($p < 0.05$) and weeks 8 ($p < 0.01$). The BV/TV, Tb.Th and Tb.N in the PGC/M40 were significantly higher than the PGC/M25 at both time points. Furthermore, the BV/TV at week 8 was significantly higher than at week 4 in PGC/M25-40 groups ($p < 0.05$). These data further demonstrated that the PGC/M40 scaffold could promote new bone formation much more strongly than the other PGC/M scaffolds.

H&E staining further verified the presence of newly-formed bone within the defects, and that the amounts of newly-formed bone increased as the increase in MBG contents (Fig. 11A). The quantitative

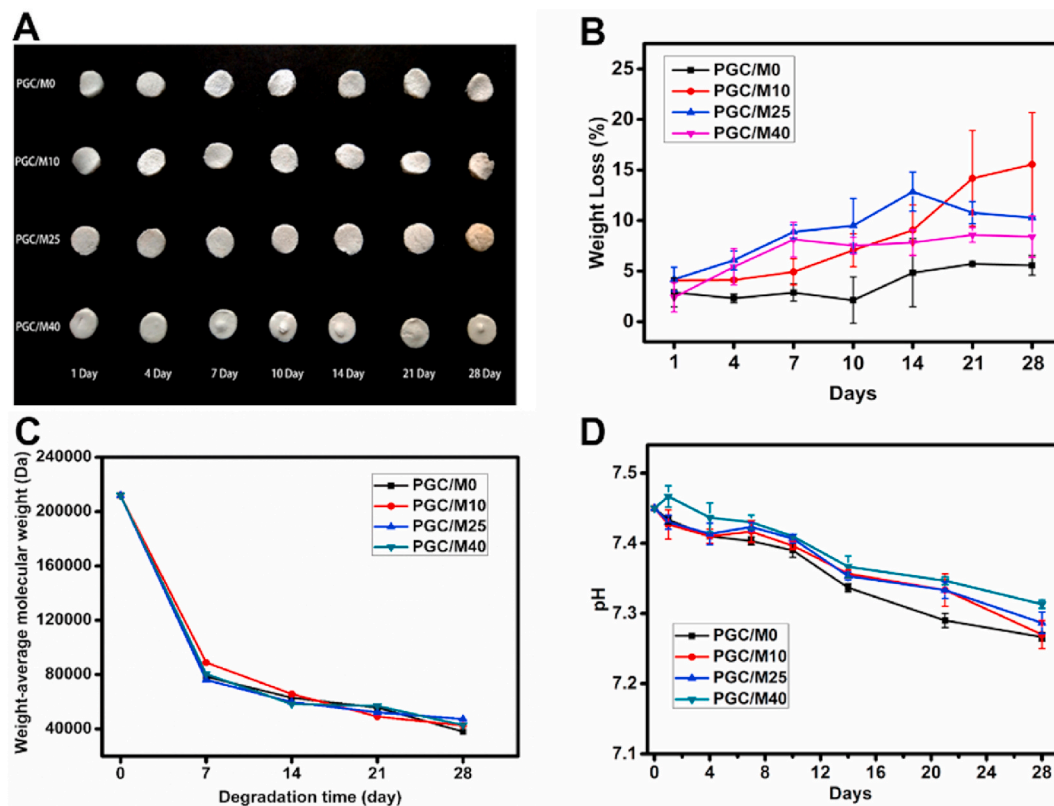


Fig. 4. In vitro degradation of PGC/M scaffolds during 4 weeks of PBS immersion. (A) Macroscopic images of the PGC/M scaffolds at 4 weeks. (B) Percentage of weight loss of the PGC/M scaffolds. (C) Changes of weight-average molecular weight (Mw) of PGA-PCL component. (D) pH value of the degradative medium.

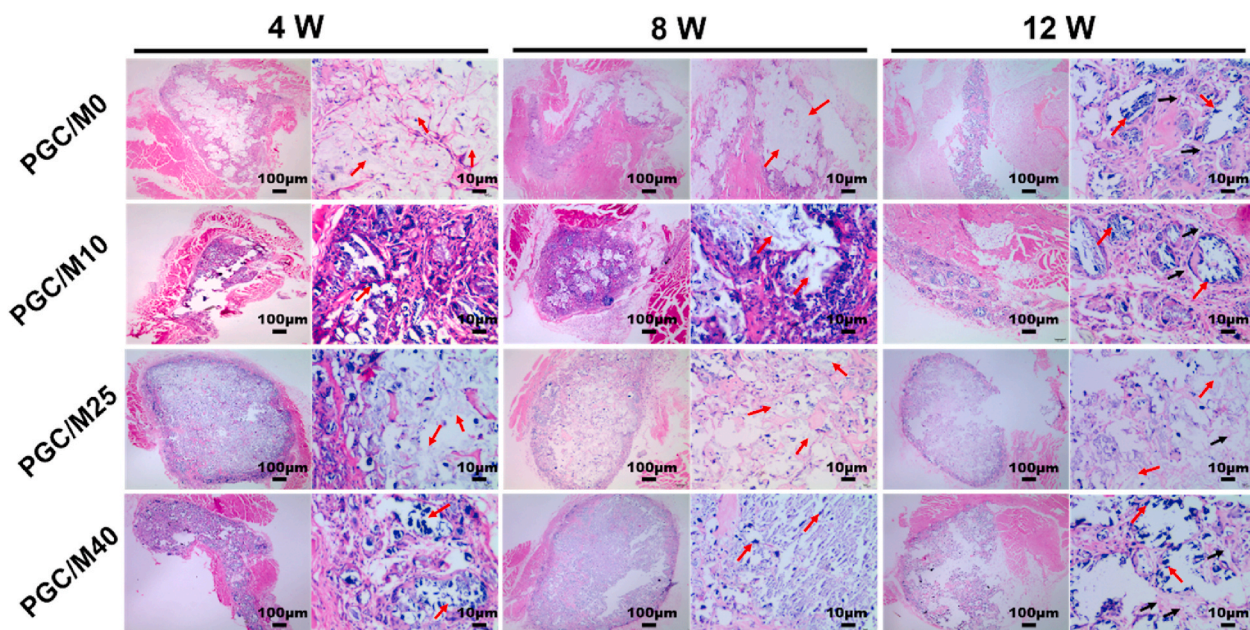


Fig. 5. Histological sections of different PGC/M scaffolds at different period of muscle implantation. Red arrows represent remaining scaffolds. Black arrows represent signs of vascularization. (For interpretation of the references to color in this figure legend, the reader is referred to the Web version of this article.)

results (Fig. 11B) showed that, at weeks 8, PGC/M40 group presented more new bone in the defects compared with the PGC/M25 group ($p < 0.05$) and especially the PGC/M0-10 and control groups ($p < 0.001$). Masson staining showed that blue-stained immature bone mainly presented at the defect edge in PGC/M0-10 groups but was also found in the defect center in PGC/M25-40 scaffolds, and red-stained mature bone

was only visible in PGC/M25-40 groups. In general, the histology examination corresponded with the Micro-CT data.

Additionally, the percentage of remanent PGC/M scaffolds significantly decreased with the increase of MBG contents (Fig. 11C). The percentage of PGC/M40 material biodegradation in the defects was about 70–80%, which was close to the percentage of newly-formed bone

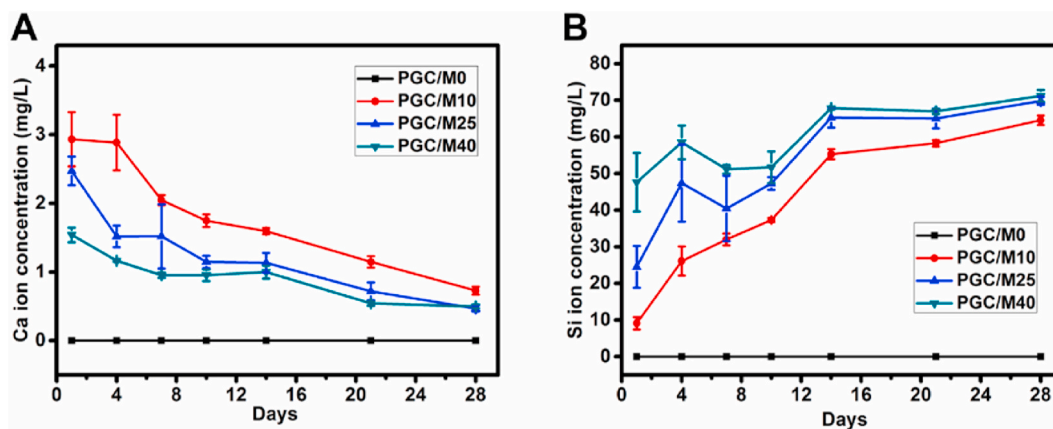


Fig. 6. Concentration of (A) Ca and (B) Si ions in the scaffold immersion solution over time.

(about 55–70%, Figs. 10B and 11B). These results indicated that the biodegradation rate of PGC/M scaffolds allowed a more rapid replacement and osteogenesis with the increase of MBG contents.

4. Discussion

Tissue-engineered bone is regarded as the most potential candidate to replace autograft in clinical practice. The scaffolds play an important role in supporting cells activity and new bone formation [4]. The composite scaffolds of polymers and inorganic bioactive materials have been considered an ideal system due to combined advantages of each individual material [14,35]. Our previous data suggested di-block PGA-PCL polymer with a 30/70 (PGA/PCL) ratio as an appropriate polymer component. For the first time, the PGC/M scaffold was constructed as a bone regeneration material.

Mechanical stirring, ultrasonic treatment [30,31,36,37], as well as surface modification [38] are common methods to evenly disperse inorganic materials into polymers, which is key to prepare homogeneous composite scaffolds. Surface modification, however, usually involves the introduction of other chemicals and their potential toxicity. Our results (Fig. 2A and B) indicated that mechanical stirring over 12 h was effective in uniformly dispersing MBG powders into PGA-PCL. Although MBG resulted in some pore collapse at high incorporation ratio, the PGC/M scaffolds still maintained the favorable large-pore structure and high porosity and connectivity (Fig. 2A). Therefore, physical treatment is a safe way to synthesize uniform composites (inorganic/polymer materials) for biomedical application.

The polymer materials possess poor cytocompatibility due to the hydrophobicity of polymers [10–14]. MBG possess high surface area and special pore structures [27,28]. Our data showed that MBG served as an effective modifier to increase scaffold performance in surface wettability, which was mainly due to the even distribution of hydrophilic MBG on the hydrophobic surface of PGA-PCL mats and scaffolds (Fig. 2A), improving the capacity of surface water absorption for PGA-PCL mats and scaffolds. The improved surface wettability would promote the interactions between the PGC/M scaffolds and cells, and further improved the cytocompatibility of PGC/M scaffolds [23,24].

The weight loss of PGC/M scaffolds increased after the incorporation of MBG while the *Mw* of PGA-PCL remained unchanged (Fig. 4 B, C), indicating that the different weight loss among PGC/M scaffolds was mainly attributed to the MBG dissolution and the deposition of hydroxyapatite crystals [39]. Previous studies reported that the incorporation of inorganic materials such as HA, BG into polymer matrix delayed the decrease in polymer *Mw* by buffering the pH changes caused acidic degradation products [17,39,40], which was contrary to our observations. The potential reason was probably attributed to a mutual canceling effect between the increasing hydrophilicity, enhancing

PGA-PCL degradation, and the improved pH stability, decreasing its degradation, due to the incorporation of MBG [39].

Since the degradation of PGC/M scaffolds was accelerated by the increase in MBG contents (Figs. 5, 10A and 11C), it is feasible to match the scaffold degradation and new bone formation by tailoring the proportion inorganic components. The accelerated degradation of PGC/M scaffolds *in vivo* might be attributed to three major aspects: 1) the increased MBG significantly improved the hydrophilicity of PGC/M scaffolds (Fig. 3 C, D), facilitating tissue fluids to penetrate the polymers and chemically attack the polymer chains [8,17,39]. 2) Enhanced cytocompatibility means more enzymes secreted by attached cells that contributes to polymer degradation [17,41]. 3) The incorporated MBG alleviated the decrease in pH values caused by the degradation of PGA-PCL, which was beneficial to increasing cell viability on scaffolds and further accelerated the degradation of PGC/M scaffolds.

Apatite formation on the scaffold surface has been considered as an important indicator to material bioactivity and subsequent *in-vivo* performance [11]. MBG incorporation significantly enhanced apatite-formation on PGC/M scaffolds in a dose-dependent manner (Fig. 7A–C). According to the mechanism of apatite formation on silicate bioactive glass [26,42,43], it was reasonable to speculate that the incorporated MBGs released Ca ions to exchange with H^+ and H_3O^+ and some Si–OH (silanol) bonds formed on its surface. The polycondensation of $Si(OH)_4$ on scaffolds-solution interfaces formed numerous SiO_2 -rich layer upon which heterogeneous nucleation and the crystallisation of a biologically reactive apatite layer could occur [11,26,42,43], inducing more apatite deposition on the surface of PGC/M scaffolds by the consumption of Ca^{2+} and PO_4^{3-} . This speculation was supported by the decreased Ca ion concentration, assigning to the apatite formation, and the increased Si ion concentration, attributing to the MBG dissolution, in the immersion PBS over time (Fig. 6 A and B), as well as the pronounced pH rise. The higher pH value associated with more MBG content might also be due to the exchange of released Ca ions with H^+ and H_3O^+ [42, 43].

Attachment is the first cell-material interactions and influences subsequent migration, proliferation and differentiation [12]. MBG incorporation increased the hydrophilicity and surface roughness of PGC/M scaffolds (Figs. 3C and 2A), which attracted more adsorbed proteins including fibronectin and vitronectin abundant in the serum to the surface of scaffolds, providing larger amount of attachment sites for cells [44–46]. This might contribute to our observation that incorporation of MBG into PGA-PCL evidently enhanced rBMSCs attachment, proliferation and viability on scaffolds (Fig. 8).

MBG is of proven superior biocompatibility and osteoinductivity [27, 28]. Our data proved that the osteoinductive property of MBG was maintained after incorporation with polymer. The most commonly used *in vitro* assays to determine osteogenic mineralization (e.g. Alizarin red

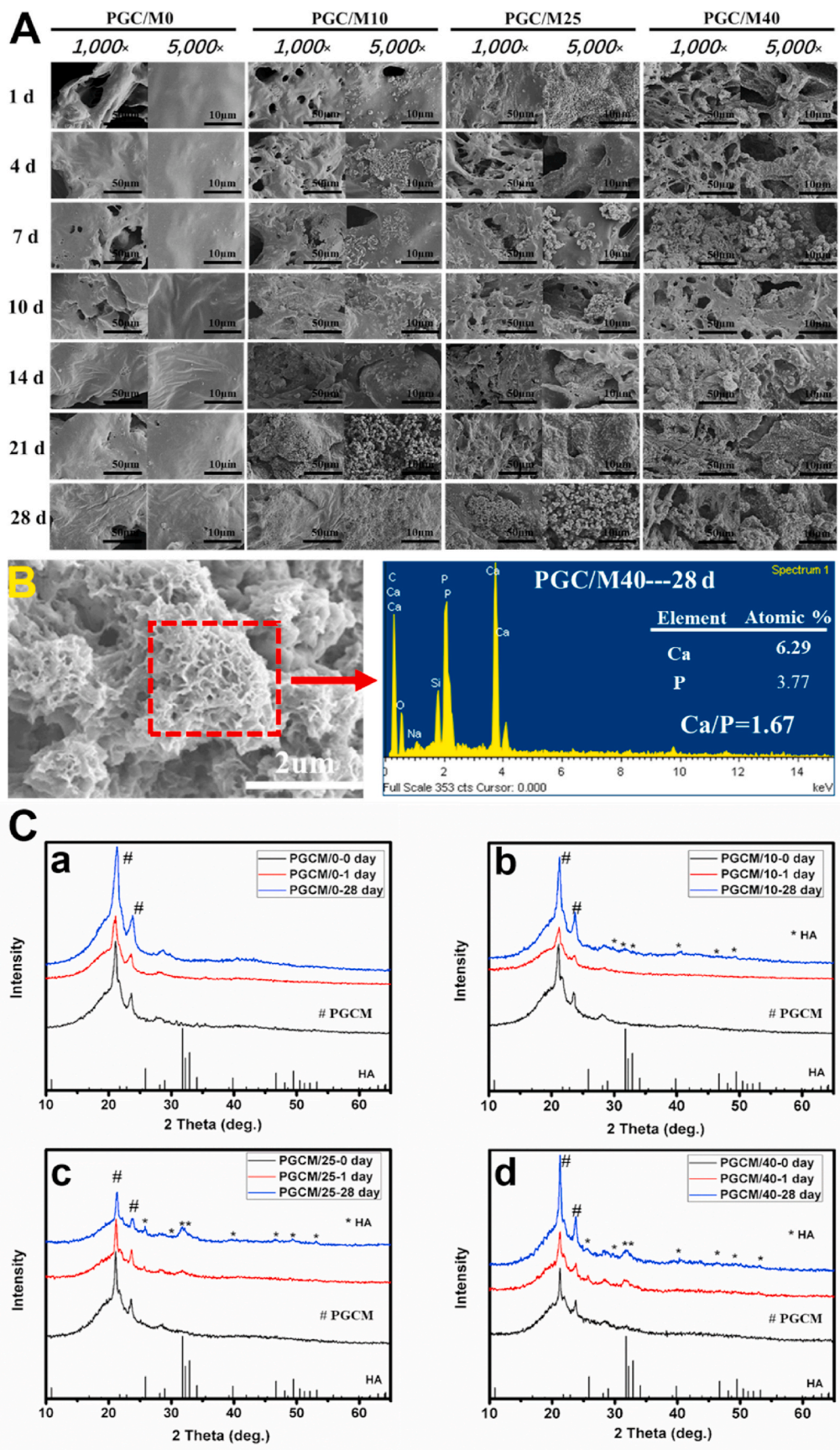


Fig. 7. Characterization of in vitro bioactivity of PGC/M scaffolds after degradation in PBS. (A) SEM images of the four PGC/M scaffolds at different time points. (B) SEM and EDS analysis of lamellar particles on PGC/M40 surface at 28 days. (C) XRD analysis of the surface particles of PGC/M scaffolds after degradation for 0, 1 and 28 days: (a) PGC/M0; (b) PGC/M10; (c) PGC/M25; (d) PGC/M40.

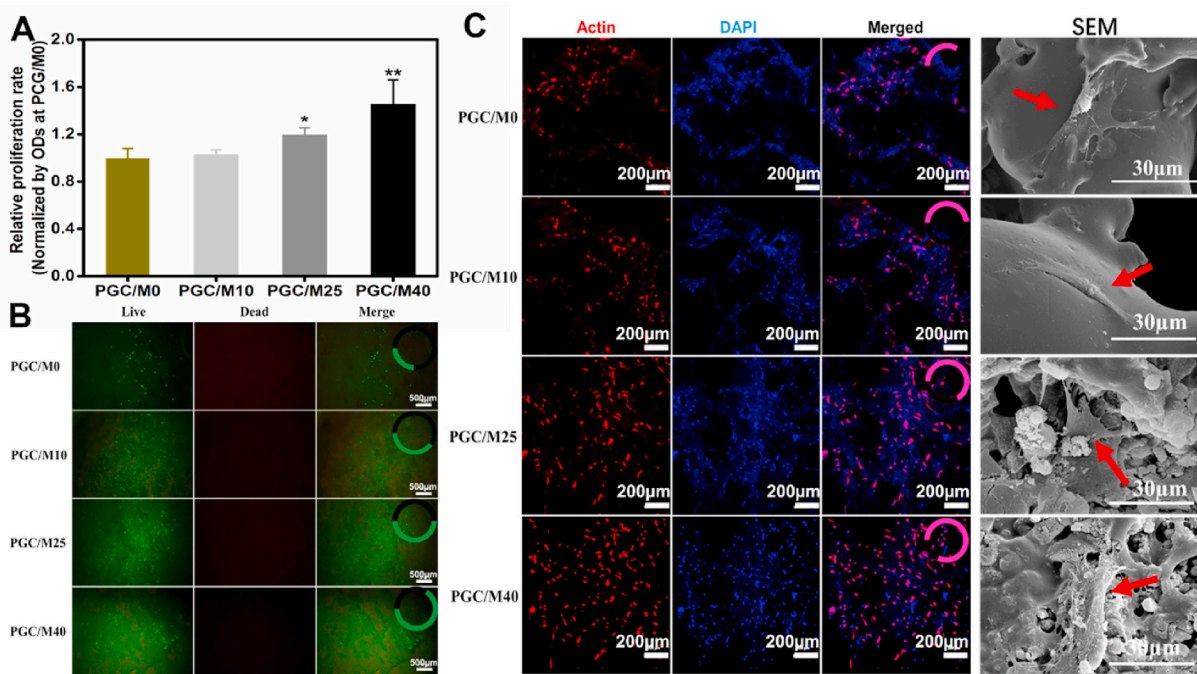


Fig. 8. Proliferation, viability and morphology features of rBMSCs on PGC/M scaffolds. (A) Relative cell proliferation rates on various PGC/M scaffolds (* $p < 0.05$, ** $p < 0.01$ VS. the PGC/M0 group) (B) Cell viability on PGC/M scaffolds after 48 h incubation. Live cells were stained into green color and dead cell were stained in red. (Green part of ring represents the proportion of fluorescence intensity of live cells) (C) Cytoskeletal morphology of rBMSCs on different PGC/M scaffolds after 72 h co-culture. Cytoskeleton stained with FITC-phalloidin (red), and cellular nuclei stained with DAPI (blue). (Pink part of ring represents the proportion of fluorescence intensity of cells and red arrows represent the cells on scaffolds.). (For interpretation of the references to color in this figure legend, the reader is referred to the Web version of this article.)

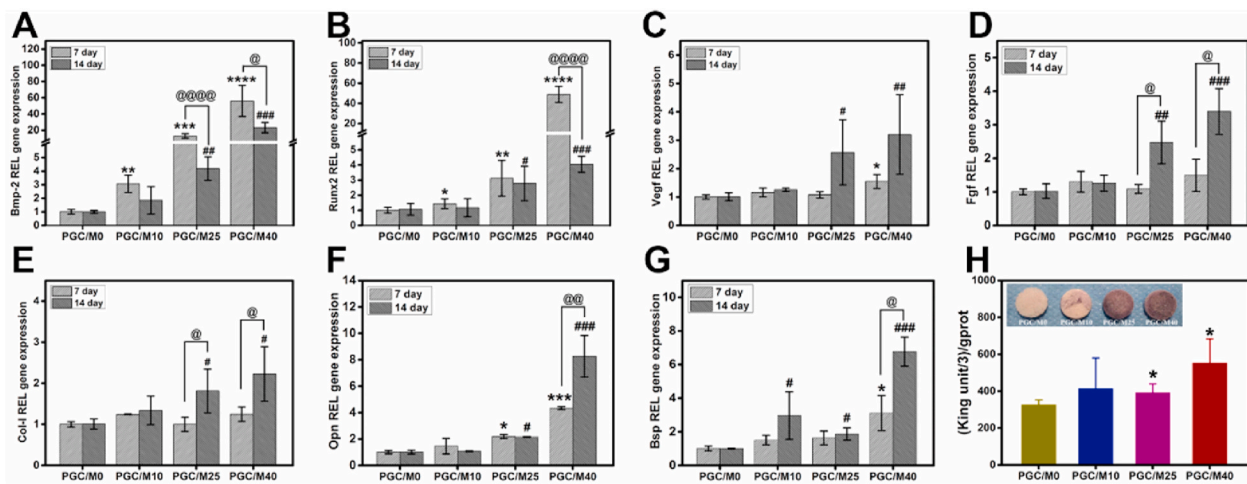


Fig. 9. Results of osteogenic activity of rBMSCs cultured on different PGC/M scaffolds for 7 and 14 days. Relative expression of related osteogenic genes: (A) Bmp-2, (B) Runx2, (C) Vegf, (D) Fgf, (E) Col-I, (F) Opn and (G) Bsp. The data are relative expression levels shown as the fold difference compared to the PGC/M0 group and are normalized to the expression level of the housekeeping gene (GAPDH). (H) ALP activity of rBMSCs cultured on various scaffolds for 7 days. (* $p < 0.05$, ** $p < 0.01$, *** $p < 0.001$, **** $p < 0.0001$ VS. the PGC/M0 group at 7 day; # $p < 0.05$, ## $p < 0.01$, ### $p < 0.001$ VS. the PGC/M0 group at 14 day; @ $p < 0.05$, @@ $p < 0.01$, @@@ $p < 0.001$ VS. the relative PGC/M25 or PGC/M40 group at 7 day).

S, which stains phosphate and calcium, respectively) were not used in our cell culture studies since the PGC/M10-40 scaffolds all contained large amounts of calcium and phosphate ions, which can interfere with the result. As a result, osteogenesis-related gene expression and ALP activity (Fig. 9) were used to quantify the extent of cell differentiation between the different PGC/M materials. The supreme expression of osteogenic genes and ALP activity in PGC/M40 group demonstrated the evidently improved osteogenic differentiation of rBMSCs on PGC/M40 scaffold. Specially, the improved expression of genes (Runx2, Col-I,

Opn) and ALP activity indicated the promotion of early osteogenic differentiation of rBMSCs on PGC/M40 scaffold. Moreover, the MBG incorporation enhanced expression level of Bmp2 and Runx2 genes more than other examined genes (Fig. 9), suggesting that MBG enhanced early osteogenic differentiation mainly via inducing multipotent mesenchymal progenitor cells to osteoblastic differentiation [47,48].

Bsp is an acidic, noncollagenous glycoprotein abundantly expressed in osteoblasts and also is a marker of osteoblast differentiation and the onset of mineral formation [49]. The significant upregulation of BSP

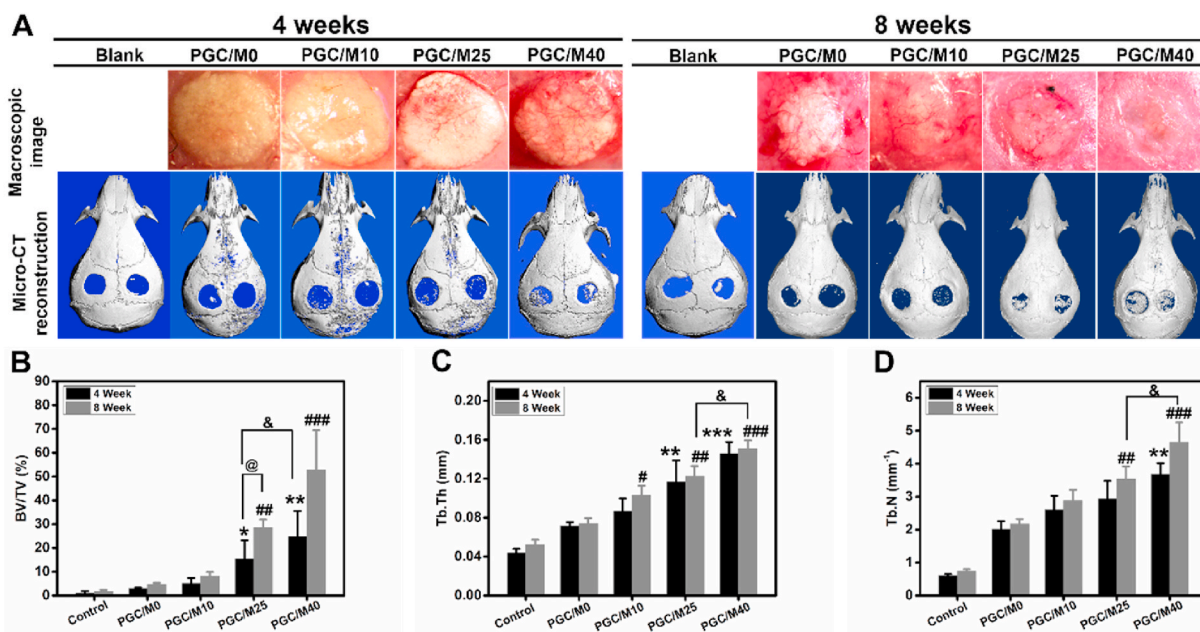


Fig. 10. Effect of different PGC/M scaffolds on bone repair of cranial defect of rats at 4 and 8 weeks. (A) Macroscopic images of implanted scaffolds and Micro-CT three-dimensional reconstruction images at defect sites. (B) Bone amounts of newly-formed bone (BV/TV, BV-the newly-formed bone volume, TV-the total volume). (C) Trabecular thickness (Tb.Th) and (D) Trabecular number of newly-formed bone (Tb.N) (* $p < 0.05$, ** $p < 0.01$ VS. the PGC/M0 and PGC/M10 groups at 4 week; ## $p < 0.01$, ### $p < 0.001$ VS. the PGC/M0 and PGC/M10 groups at 8 week; @ $p < 0.05$, & $p < 0.05$).

gene expression at 14 days for PGC/M40 group ($p < 0.001$) suggested that the high content of incorporated MBG also promoted the late osteogenic differentiation of rBMSCs in non-osteoinductive media compared to PGC/M0 group.

FGF is a multipotent cell growth factor and can promote the proliferation of MSCs and the differentiation of MSCs into osteoblasts, accelerates endochondral ossification, thus increasing the amount of bone formation [50]. The promoting effect of PGC/M40 scaffold on the proliferation and osteogenic differentiation of rBMSCs might be partly acquired by upregulating Fgf gene expression (Fig. 9D) or stimulating Fgf-related gene/protein expression after the initiation of osteoinduction due to upregulation of Bmp-2 gene expression [50]. Besides, Fgf also could promote the vascularization of bone grafts by the upregulation of Vegf expression to facilitate newly-formed bone [51]. The upregulated Vegf expression (Fig. 9C) suggested that the incorporated MBG improved the potential of the angiogenesis on PGC/M40 scaffold, which probably also was related to the upregulation of Fgf gene expression [51]. Further comprehensive investigations are warranted to explore the role of Fgf in osteogenesis of rBMSCs cultured on PGC/M scaffolds.

Our previous study demonstrated that Si ions released from MBG synergistically promoted the osteogenic differentiation of rBMSCs with Ca, P ions via the activation of Itga 2b-pFAK-MAPK (pERK1/2 and pP38) signaling pathway [52]. The dissolution of MBG in the PGC/M scaffold releases free Si, Ca and P ions and may stimulates cell response in a similar way [53–55].

Our in vivo results suggested a strong dose-dependent correlation between MBG incorporation ratio and osteoinductive performance (Figs. 10 and 11). The in vivo pro-osteogenic effect of PGC/M scaffolds could be attributed to the following aspects: (1) MBG incorporation significantly improved the scaffold hydrophilicity and cytocompatibility [44–46]. (2) MBG induced more blood vessels growing into the scaffolds (Fig. 10A), which might be attributed to the activation of angiogenesis-related genes (FGF and VEGF) (Fig. 9C and D) [50,51], bringing more osteogenesis-related cells and better nutrients exchange and waste removal [56]. (3) The dissolution of MBG continuously released bioactive ions. (4) The embedded MBG induced hydroxyapatite

formation on the surface of scaffolds and strengthened the interactions between the scaffolds and the newly-formed bone [25].

MBG incorporation accelerated the biodegradability of PGC/M scaffolds and evidently promoted the newly-formed bone at defect sites. The in vivo results demonstrated that a good balance between biodegradability and osteogenic capacity in PGC/M bone grafts was achieved by adjusting the contents of incorporated MBG.

5. Conclusion

In this study, the synthesized MBG particles presented the worm-like morphology, possessed a high long-rang ordered mesoporous structure, and exhibited the high specific surface. The prepared PGC/M scaffolds possessed a highly uniform macropore structure with a 300–450 μm pore size. The incorporated MBG was uniformly dispersed in PGC/M scaffolds. The PGC/M10-40 scaffolds had the better hydrophilicity, bioactivity, degradation, cytocompatibility and osteogenic activity in vitro and furthermore, exhibited a faster degradation rate and a better bone repair effect in vivo compared to the PGC/M0 scaffold, in which PGC/M40 scaffold presented the optimal effect. Moreover, these properties of PGC/M scaffolds could be tailored by adjusting the incorporation of MBG contents to meet different bone repairing circumstances. These data supported that MBG/PGA-PCL composite serves as a highly tunable platform for the development of bone substitutes, meeting diverse bony repair circumstances with tailored biodegradation and osteogenic features.

CRedit authorship contribution statement

Jiangfeng Li: Conceptualization, Methodology, Investigation, Formal analysis, Resources, Visualization, Writing – original draft, Project administration, Writing – review & editing. **Chunyi Wang:** Methodology, Investigation. **Guoxing Gao:** Investigation. **Xing Yin:** Resources, Writing – review & editing. **Ximing Pu:** Resources, Data curation. **Bing Shi:** Funding acquisition, Resources, Project administration, Supervision. **Yang Liu:** Resources. **Zhongbing Huang:** Conceptualization, Methodology, Project administration. **Juan Wang:**

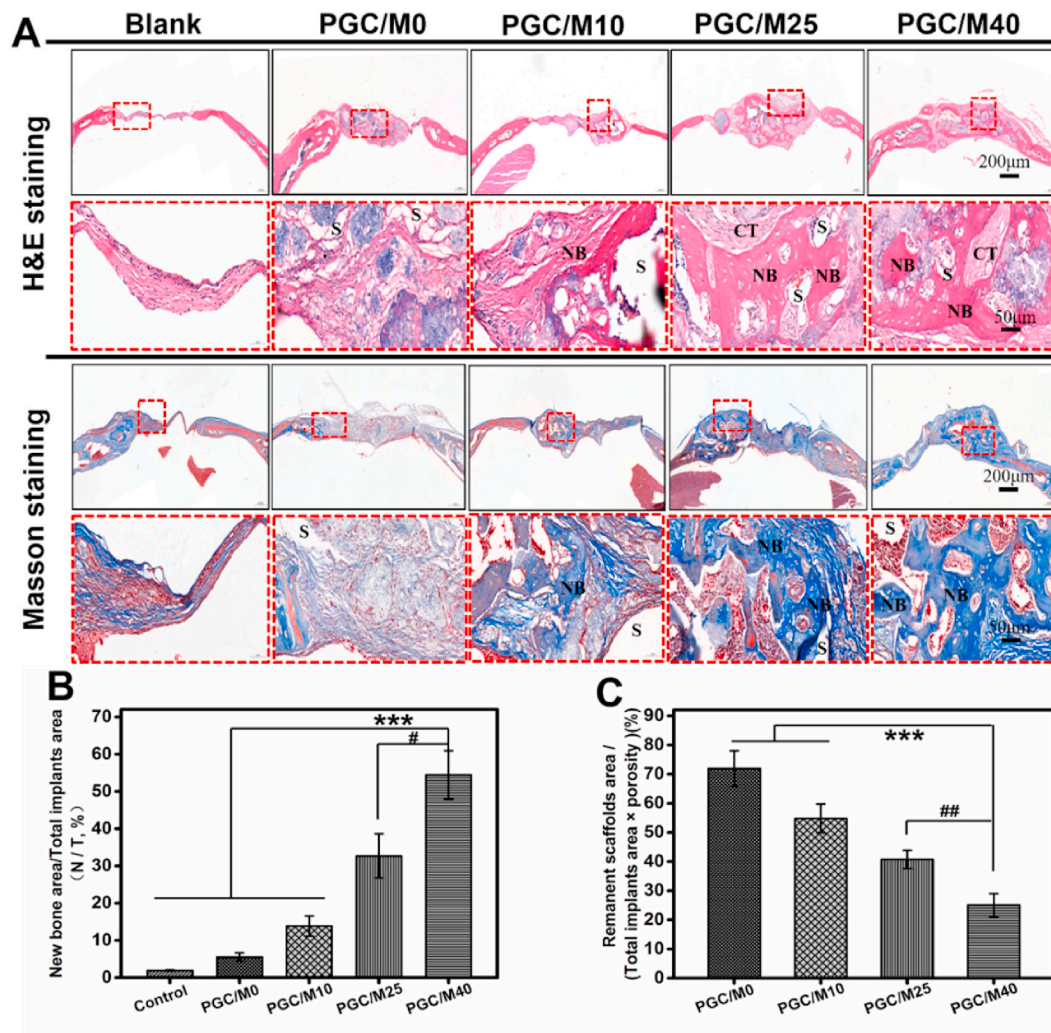


Fig. 11. Histological analysis of the decalcified sections of bone defects. (A) Representative images of H&E and Masson staining at weeks 8 (NB represents newly formed bone, CT represents connective tissue, S represents implanted scaffolds). (B) New bone area quantified at week 8. (C) Remanent scaffold materials quantified at week 8. (** $p < 0.001$; # $p < 0.05$, ## $p < 0.01$; $n = 4$).

Resources, Data curation, Visualization. **Jingtao Li:** Conceptualization, Methodology, Investigation, Resources, Writing – review & editing. **Guangfu Yin:** Conceptualization, Funding acquisition, Resources, Project administration, Supervision, Writing – review & editing.

Declaration of competing interest

The authors declare that they have no known competing financial interests or personal relationships that could have appeared to influence the work reported in this paper.

Acknowledgements

This work was supported by National Key R & D Program of China (2018YFC1105703) and Key R & D Program of Sichuan Province (2017SZ0047).

Appendix A. Supplementary data

Supplementary data to this article can be found online at <https://doi.org/10.1016/j.bioactmat.2021.11.034>.

References

- [1] J.A. Peres, T. Lamano, Strategies for stimulation of new bone formation: a critical review, *Braz. Dent. J.* 22 (2011), <https://doi.org/10.1590/S0103-64402011000600001>.
- [2] P.S.P. Poh, D.W. Huttmacher, B.M. Holzapfel, A.K. Solanki, M.M. Stevens, M. A. Woodruff, In vitro and in vivo bone formation potential of surface calcium phosphate-coated polycaprolactone and polycaprolactone/bioactive glass composite scaffolds, *Acta Biomater.* 30 (2016), <https://doi.org/10.1016/j.actbio.2015.11.012>.
- [3] S. Wu, X. Liu, K.W.K. Yeung, C. Liu, X. Yang, Biomimetic porous scaffolds for bone tissue engineering, *Mater. Sci. Eng. R Rep.* 80 (2014), <https://doi.org/10.1016/j.mser.2014.04.001>.
- [4] D.W. Huttmacher, Scaffolds in tissue engineering bone and cartilage, *Biomaterials* 21 (2000), [https://doi.org/10.1016/S0142-9612\(00\)00121-6](https://doi.org/10.1016/S0142-9612(00)00121-6).
- [5] W.G. De Long, T.A. Einhorn, K. Koval, M. McKee, W. Smith, R. Sanders, T. Watson, Bone grafts and bone graft substitutes in orthopaedic trauma surgery, *J. Bone Jt. Surg.* 89 (2007), <https://doi.org/10.2106/jbjs.f.00465>.
- [6] P.A. Gunatillake, R. Adhikari, N. Gadegaard, Biodegradable synthetic polymers for tissue engineering, *Eur. Cell. Mater.* 5 (2003), <https://doi.org/10.22203/eCM.v005a01>.
- [7] C. Bertoldi, D. Zaffe, U. Consolo, Poly(lactide)/poly(glycolide) copolymer in bone defect healing in humans, *Biomaterials* 29 (2008), <https://doi.org/10.1016/j.biomaterials.2007.12.034>.
- [8] G. Storti, M. Lattuada, Synthesis of bioresorbable polymers for medical applications, in: *Bioresorbable Polym. Biomed. Appl. From Fundam. To Transl. Med.*, 2017, <https://doi.org/10.1016/B978-0-08-100262-9.00008-2>.
- [9] X. Zhang, X. Peng, S.W. Zhang, Synthetic biodegradable medical polymers: polymer blends, in: *Sci. Princ. Biodegrad. Bioresorbable Med. Polym. Mater. Prop.*, 2017, <https://doi.org/10.1016/B978-0-08-100372-5.00007-6>.

- [10] S. Chen, Z. Jian, L. Huang, W. Xu, S. Liu, D. Song, Z. Wan, A. Vaughn, R. Zhan, C. Zhang, S. Wu, M. Hu, J. Li, Mesoporous bioactive glass surface modified poly (lactic-co-glycolic acid) electrospun fibrous scaffold for bone regeneration, *Int. J. Nanomed.* 10 (2015), <https://doi.org/10.2147/IJN.S82543>.
- [11] C. Wu, Y. Ramaswamy, Y. Zhu, R. Zheng, R. Appleyard, A. Howard, H. Zreiqat, The effect of mesoporous bioactive glass on the physicochemical, biological and drug-release properties of poly(DL-lactide-co-glycolide) films, *Biomaterials* 30 (2009), <https://doi.org/10.1016/j.biomaterials.2009.01.029>.
- [12] H.M. Lin, Y.H. Lin, F.Y. Hsu, Preparation and characterization of mesoporous bioactive glass/polycaprolactone nanofibrous matrix for bone tissues engineering, *J. Mater. Sci. Mater. Med.* 23 (2012), <https://doi.org/10.1007/s10856-012-4734-z>.
- [13] J. Wei, F. Chen, J.W. Shin, H. Hong, C. Dai, J. Su, C. Liu, Preparation and characterization of bioactive mesoporous wollastonite - polycaprolactone composite scaffold, *Biomaterials* 30 (2009), <https://doi.org/10.1016/j.biomaterials.2008.10.046>.
- [14] H. Cao, N. Kuboyama, A biodegradable porous composite scaffold of PGA/ β -TCP for bone tissue engineering, *Bone* 46 (2010), <https://doi.org/10.1016/j.bone.2009.09.031>.
- [15] N. Hild, P.N. Tawakoli, J.G. Halter, B. Sauer, W. Buchalla, W.J. Stark, D. Mohn, pH-dependent antibacterial effects on oral microorganisms through pure PLGA implants and composites with nanosized bioactive glass, *Acta Biomater.* 9 (2013), <https://doi.org/10.1016/j.actbio.2013.06.030>.
- [16] L. Lu, S.J. Peter, M.D. Lyman, H.L. Lai, S.M. Leite, J.A. Tamada, S. Uyama, J. P. Vacanti, Robert Langer, A.G. Mikos, In vitro and in vivo degradation of porous poly(DL-lactic-co-glycolic acid) foams, *Biomaterials* 21 (2000), [https://doi.org/10.1016/S0142-9612\(00\)00047-8](https://doi.org/10.1016/S0142-9612(00)00047-8).
- [17] N. Zhang, H.L. Nichols, S. Tylor, X. Wen, Fabrication of nanocrystalline hydroxyapatite doped degradable composite hollow fiber for guided and biomimetic bone tissue engineering, *Mater. Sci. Eng. C* 27 (2007), <https://doi.org/10.1016/j.msec.2006.05.024>.
- [18] P. Zhang, Z. Hong, T. Yu, X. Chen, X. Jing, In vivo mineralization and osteogenesis of nanocomposite scaffold of poly(lactide-co-glycolide) and hydroxyapatite surface-grafted with poly(L-lactide), *Biomaterials* 30 (2009), <https://doi.org/10.1016/j.biomaterials.2008.08.041>.
- [19] M.V. Jose, V. Thomas, K.T. Johnson, D.R. Dean, E. Nyairo, Aligned PLGA/HA nanofibrous nanocomposite scaffolds for bone tissue engineering, *Acta Biomater.* 5 (2009), <https://doi.org/10.1016/j.actbio.2008.07.019>.
- [20] Y. Ma, W. Zhang, Z. Wang, Z. Wang, Q. Xie, H. Niu, H. Guo, Y. Yuan, C. Liu, PEGylated poly(glycerol sebacate)-modified calcium phosphate scaffolds with desirable mechanical behavior and enhanced osteogenic capacity, *Acta Biomater.* 44 (2016), <https://doi.org/10.1016/j.actbio.2016.08.023>.
- [21] S. Lin, L. Cui, G. Chen, J. Huang, Y. Yang, K. Zou, Y. Lai, X. Wang, L. Zou, T. Wu, J. C.Y. Cheng, G. Li, B. Wei, W.Y.W. Lee, PLGA/ β -TCP composite scaffold incorporating salvianolic acid B promotes bone fusion by angiogenesis and osteogenesis in a rat spinal fusion model, *Biomaterials* 196 (2019), <https://doi.org/10.1016/j.biomaterials.2018.04.004>.
- [22] S.H. Chen, M. Lei, X.H. Xie, L.Z. Zheng, D. Yao, X.L. Wang, W. Li, Z. Zhao, A. Kong, D.M. Xiao, D.P. Wang, X.H. Pan, Y.X. Wang, L. Qin, PLGA/TCP composite scaffold incorporating bioactive phytomolecule icaritin for enhancement of bone defect repair in rabbits, *Acta Biomater.* 9 (2013), <https://doi.org/10.1016/j.actbio.2013.01.024>.
- [23] A.M. Haaparanta, P. Uppstu, M. Hannula, V. Ellä, A. Rosling, M. Kellomäki, Improved dimensional stability with bioactive glass fibre skeleton in poly(lactide-co-glycolide) porous scaffolds for tissue engineering, *Mater. Sci. Eng. C* 56 (2015), <https://doi.org/10.1016/j.msec.2015.07.013>.
- [24] L. Yang, S. Liu, W. Fang, J. Chen, Y. Chen, Poly(lactic-co-glycolic acid)-bioactive glass composites as nanoporous scaffolds for bone tissue engineering: in vitro and in vivo studies, *Exp. Ther. Med.* 18 (6) (2019) 4874–4880, <https://doi.org/10.3892/etm.2019.8121>.
- [25] C. Wu, J. Chang, Mesoporous bioactive glasses: structure characteristics, drug/growth factor delivery and bone regeneration application, *Interf. Focus* 2 (2012), <https://doi.org/10.1098/rsfs.2011.0121>.
- [26] X. Yan, X. Huang, C. Yu, H. Deng, Y. Wang, Z. Zhang, S. Qiao, G. Lu, D. Zhao, The in-vitro bioactivity of mesoporous bioactive glasses, *Biomaterials* 27 (2006), <https://doi.org/10.1016/j.biomaterials.2006.01.043>.
- [27] C. Wu, J. Chang, Multifunctional mesoporous bioactive glasses for effective delivery of therapeutic ions and drug/growth factors, *J. Contr. Release* 193 (2014), <https://doi.org/10.1016/j.jconrel.2014.04.026>.
- [28] J. Li, X. Li, J. Li, X. Pu, J. Wang, Z. Huang, G. Yin, Effects of incorporated vanadium and its chemical states on morphology and mesostructure of mesoporous bioactive glass particles, *Microporous Mesoporous Mater.* 319 (2021), <https://doi.org/10.1016/j.micromeso.2021.111061>.
- [29] M. Shi, D. Zhai, L. Zhao, C. Wu, J. Chang, Nanosized mesoporous bioactive glass/poly(lactic-co-glycolic acid) composite-coated CaSiO₃ scaffolds with multifunctional properties for bone tissue engineering, *BioMed Res. Int.* 2014 (2014), <https://doi.org/10.1155/2014/323046>.
- [30] N. Gómez-Cerezo, L. Casarrubios, M. Saiz-Pardo, L. Ortega, D. de Pablo, I. Díaz-Güemes, B. Fernández-Tomé, S. Enciso, F.M. Sánchez-Margallo, M.T. Portolés, D. Arcos, M. Vallet-Regí, Mesoporous bioactive glass/e-polycaprolactone scaffolds promote bone regeneration in osteoporotic sheep, *Acta Biomater.* 90 (2019), <https://doi.org/10.1016/j.actbio.2019.04.019>.
- [31] X. Li, J. Shi, X. Dong, L. Zhang, H. Zeng, A mesoporous bioactive glass/polycaprolactone composite scaffold and its bioactivity behavior, *J. Biomed. Mater. Res.* 84 (2008), <https://doi.org/10.1002/jbm.a.31371>.
- [32] E. Karaoz, A. Aksoy, S. Ayhan, A.E. Sariboyaci, F. Kaymaz, M. Kasap, Characterization of mesenchymal stem cells from rat bone marrow: ultrastructural properties, differentiation potential and immunophenotypic markers, *Histochem. Cell Biol.* 132 (2009), <https://doi.org/10.1007/s00418-009-0629-6>.
- [33] X. Yan, C. Yu, X. Zhou, J. Tang, D. Zhao, Highly ordered mesoporous bioactive glasses with superior in vitro bone-forming bioactivities, *Angew. Chem. Int. Ed.* 43 (2004), <https://doi.org/10.1002/anie.200460598>.
- [34] C. Dhand, S.T. Ong, N. Dwivedi, S.M. Diaz, J.R. Venugopal, B. Navaneethan, M.H. U.T. Fazil, S. Liu, V. Seitz, E. Wintermantel, R.W. Beuerman, S. Ramakrishna, N. K. Verma, R. Lakshminarayanan, Bio-inspired in situ crosslinking and mineralization of electrospun collagen scaffolds for bone tissue engineering, *Biomaterials* 104 (2016), <https://doi.org/10.1016/j.biomaterials.2016.07.007>.
- [35] S. Bose, M. Roy, A. Bandyopadhyay, Recent advances in bone tissue engineering scaffolds, *Trends Biotechnol.* 30 (2012), <https://doi.org/10.1016/j.tibtech.2012.07.005>.
- [36] P. Zhang, Z. Hong, T. Yu, X. Chen, X. Jing, In vivo mineralization and osteogenesis of nanocomposite scaffold of poly(lactide-co-glycolide) and hydroxyapatite surface-grafted with poly(L-lactide), *Biomaterials* 30 (2009), <https://doi.org/10.1016/j.biomaterials.2008.08.041>.
- [37] X. Han, D. Wang, X. Chen, H. Lin, F. Qu, One-pot synthesis of macro-mesoporous bioactive glasses/poly(lactic acid) for bone tissue engineering, *Mater. Sci. Eng. C* 43 (2014), <https://doi.org/10.1016/j.msec.2014.07.042>.
- [38] N. Abouzadeh, M. Imani, M.A. Shokrgozar, A. Khavandi, J. Javadpour, Y. Shafieyan, M. Farokhi, Fabrication and characterization of poly(D,L-lactide-co-glycolide)/hydroxyapatite nanocomposite scaffolds for bone tissue regeneration, *J. Biomed. Mater. Res.* 94 (2010), <https://doi.org/10.1002/jbm.a.32673>.
- [39] I. Armentano, M. Dottori, E. Fortunati, S. Mattioli, J.M. Kenny, Biodegradable polymer matrix nanocomposites for tissue engineering: a review, in: *Polym. Degrad. Stab.*, 2010, <https://doi.org/10.1016/j.polydegradstab.2010.06.007>.
- [40] Y. Yang, S. Yang, Y. Wang, Z. Yu, H. Ao, H. Zhang, L. Qin, O. Guillaume, D. Eglin, R.G. Richards, T. Tang, Anti-infective efficacy, cytocompatibility and biocompatibility of a 3D-printed osteoconductive composite scaffold functionalized with quaternized chitosan, *Acta Biomater.* 46 (2016), <https://doi.org/10.1016/j.actbio.2016.09.035>.
- [41] J. Zhou, C. Cao, X. Ma, L. Hu, L. Chen, C. Wang, In vitro and in vivo degradation behavior of aqueous-derived electrospun silk fibroin scaffolds, *Polym. Degrad. Stab.* 95 (2010), <https://doi.org/10.1016/j.polydegradstab.2010.05.025>.
- [42] P. Saravanapavan, J.R. Jones, R.S. Pryce, L.L. Hench, Bioactivity of gel-glass powders in the CaO-SiO₂ system: a comparison with ternary (CaO-P₂O₅-SiO₂) and quaternary glasses (SiO₂-CaO-P₂O₅-Na₂O), *J. Biomed. Mater. Res.* 66 (2003), <https://doi.org/10.1002/jbm.a.10532>.
- [43] J.R. Jones, P. Sepulveda, L.L. Hench, Dose-dependent behavior of bioactive glass dissolution, *J. Biomed. Mater. Res.* 58 (2001), <https://doi.org/10.1002/jbm.10053>.
- [44] K. Rechendorff, M.B. Hovgaard, M. Foss, V.P. Zhdanov, F. Besenbacher, Enhancement of protein adsorption induced by surface roughness, *Langmuir* 22 (2006), <https://doi.org/10.1021/la0621923>.
- [45] H.W. Kim, H.E. Kim, V. Salih, Stimulation of osteoblast responses to biomimetic nanocomposites of gelatin-hydroxyapatite for tissue engineering scaffolds, *Biomaterials* 26 (2005), <https://doi.org/10.1016/j.biomaterials.2005.01.047>.
- [46] I. Degasne, M.F. Baslé, V. Demais, G. Huré, M. Lesourd, B. Grolleau, L. Mercier, D. Chappard, Effects of roughness, fibronectin and vitronectin on attachment, spreading, and proliferation of human osteoblast-like cells (Saos-2) on titanium surfaces, *Calcif. Tissue Int.* 64 (1999), <https://doi.org/10.1007/s002239906640>.
- [47] J. Yang, P. Shi, M. Tu, Y. Wang, M. Liu, F. Fan, M. Du, Bone morphogenetic proteins: relationship between molecular structure and their osteogenic activity, *Food Sci. Hum. Wellness.* 3 (2014), <https://doi.org/10.1016/j.fshw.2014.12.002>.
- [48] K. Lam, D.-E. Zhang, RUNX/CBF transcription Factors, in: *Ref. Modul. Biomed. Sci.*, 2015, <https://doi.org/10.1016/b978-0-12-801238-3.98749-x>.
- [49] J.A.R. Gordon, C.E. Tye, A.V. Sampaio, T.M. Underhill, G.K. Hunter, H. A. Goldberg, Bone sialoprotein expression enhances osteoblast differentiation and matrix mineralization in vitro, *Bone* 41 (2007), <https://doi.org/10.1016/j.bone.2007.04.191>.
- [50] J.R. Lieberman, A. Daluiski, T.A. Einhorn, The role of growth factors in the repair of bone biology and clinical applications, *J. Bone Jt. Surg. - Ser. A.* 84 (2002), <https://doi.org/10.2106/00004623-200206000-00022>.
- [51] A.B.M. Rabie, M. Lu, Basic fibroblast growth factor up-regulates the expression of vascular endothelial growth factor during healing of allogeneic bone graft, *Arch. Oral Biol.* 49 (2004), <https://doi.org/10.1016/j.archoralbio.2004.05.012>.
- [52] J. Li, J. Li, Y. Wei, N. Xu, J. Li, X. Pu, J. Wang, Z. Huang, X. Liao, G. Yin, Ion release behavior of vanadium-doped mesoporous bioactive glass particles and the effect of the released ions on osteogenic differentiation of BMSCs via the FAK/MAPK signaling pathway [J], *J. Mater. Chem. B* 9 (2021) 7848–7865, <https://doi.org/10.1039/D1TB01479J>.
- [53] A. Hoppe, N.S. Güldal, A.R. Boccaccini, A review of the biological response to ionic dissolution products from bioactive glasses and glass-ceramics, *Biomaterials* 32 (2011), <https://doi.org/10.1016/j.biomaterials.2011.01.004>.
- [54] S. Maeno, Y. Niki, H. Matsumoto, H. Morioka, T. Yatabe, A. Funayama, Y. Toyama, T. Taguchi, J. Tanaka, The effect of calcium ion concentration on osteoblast

- viability, proliferation and differentiation in monolayer and 3D culture, *Biomaterials* 26 (2005), <https://doi.org/10.1016/j.biomaterials.2005.01.006>.
- [55] P. Han, C. Wu, Y. Xiao, The effect of silicate ions on proliferation, osteogenic differentiation and cell signalling pathways (WNT and SHH) of bone marrow stromal cells, *Biomater. Sci.* 1 (2013), <https://doi.org/10.1039/c2bm00108j>.
- [56] W.C. Liu, S. Chen, L. Zheng, L. Qin, Angiogenesis assays for the evaluation of angiogenic properties of orthopaedic biomaterials – a general review, *Adv. Healthc. Mater.* 6 (2017), <https://doi.org/10.1002/adhm.201600434>.